RSC Advances

PAPER

View Article Online
View Journal | View Issue

Cite this: *RSC Adv.*, 2025, **15**, 15266

Long-term postoperative treatment of open fractures using *in situ* medicine delivery based on mesoporous MCM-41/hydrogel composites†

Yuhao Pan,[a] Peiyan Shi,[a] Liuyi Pu,[a] Donglai Song,[a] Jiaping Lu,*[c] Wenjie Hou*[b] and Kangjian Tang *[a]

Open fracture surgery is one of the common emergency procedures in orthopedics. It requires effective postoperative management, including anti-inflammatory and antimicrobial measures, as well as promotion of bone cell growth. Due to the higher risk of infection and challenges in fracture healing associated with open fractures, the development of effective long-acting postoperative therapeutic drug delivery materials is crucial. In this study, we demonstrate the development of one spontaneous administration for the postoperative maintenance and treatment of open fractures. By integrating medicine-loaded mesoporous molecular sieves (MMMSs) with hydrogels, a composite material termed nanoporous medicine composite hydrogel (NMCH) was formulated. Through adjusting the proportions of hydrogel monomers and molecular sieves, this material attained mechanical properties akin to periosteum. Physicochemical studies including XRD, SEM, TEM, UV absorption, and N_2 adsorption confirmed excellent drug-loading capabilities of the composite material. Furthermore, antibacterial experiments, cell proliferation assays, and mouse paw edema tests validated significant effects of the drug-loaded composite material in antibacterial activity, promotion of osteoblast growth, and anti-inflammatory properties, demonstrating its enormous potential and application value in postoperative treatment of open fractures.

Received 13th January 2025
Accepted 30th April 2025

DOI: 10.1039/d5ra00313j

rsc.li/rsc-advances

1. Introduction

Open fracture surgery, serving as an emergent and complex medical intervention, aims to repair bone fractures accompanied by skin breaches resulting from trauma.[1,2] In such surgeries, patients not only confront direct damage to their bone structures but also frequently encounter various postoperative complications, notably bacterial infections and inflammatory responses.[3] These complications not only prolong patients' recovery periods and increase the complexity of treatment but may also lead to long-term functional impairments and even disabilities. Given the high risks associated with open fracture surgeries and the arduous nature of subsequent management, optimizing surgical techniques, enhancing postoperative care, and implementing infection prevention measures are of paramount importance.[4,5]

Regarding the postoperative management of common open fracture surgeries, there are primarily three methods.[6,7] Firstly, systemic medications, such as oral drugs, are administered, exerting their effects through the body's circulation.[8] Secondly, topical ointments or creams are applied.[9] Lastly, intravenous injections are utilized.[10] Unfortunately, to achieve and maintain effective drug concentrations at the fracture site, oral medications often require high systemic doses, which can lead to toxic side effects, cardiovascular issues, and drug resistance.[11] On the other hand, topical ointments often struggle to maintain sufficient adhesion to the affected area, requiring frequent reapplication that may delay wound healing and exacerbate discomfort.[12] While intravenous injections are effective, they can still produce systemic side effects, and their short duration of action may necessitate repeated administrations.[13] Additionally, intravenous injections can cause discomfort and restrict patient mobility. Collectively, these traditional methods result in significant inconvenience, discomfort, and additional trauma for patients during the recovery phase, severely disrupting their daily lives and diminishing their overall quality of life. Given the intricate postoperative challenges posed by open fracture wounds and the critical importance of maintaining patient comfort throughout treatment, there is an urgent need to develop an innovative drug delivery system capable of providing targeted, prolonged, reliable, user-friendly, and potentially self-regulating medication administration directly at

[a]*Innovation Center for Chemical Sciences, College of Chemistry, Chemical Engineering and Materials Science, Jiangsu Key Laboratory of Advanced Negative Carbon Technologies, Soochow University, Suzhou 215123, People's Republic of China. E-mail: kjtang@suda.edu.cn*

[b]*Department of Gynecology and Obstetrics, The Fourth Affiliated Hospital of Soochow University, China. E-mail: wjhou@suda.edu.cn*

[c]*Dental Clinic of Xuhui District, Shanghai 200031, People's Republic of China. E-mail: natalieljp@126.com*

† Electronic supplementary information (ESI) available. See DOI: https://doi.org/10.1039/d5ra00313j

the wound site.[14–16] Precise medicine delivery systems offer numerous benefits, including enhanced therapeutic efficacy, sustained action, and reduced toxicity to organs, thereby garnering substantial interest within the medical and chemical fields.[17,18] Numerous successful delivery systems have emerged, for instance, utilizing chitosan in cancer treatment, hydrogels in managing diabetic conditions, liposomes in addressing Alzheimer's disease, and iron oxide nanoparticles in treating neoplastic disorders.[19–23] Among these, Mesoporous Silica Nanoparticles (MSNs) stand out as a highly promising material for drug delivery, owing to their customizable pore size, extensive surface area, easily modifiable surface, and superior biocompatibility.[24] Illustrative applications encompass their integration with hydrogels for treating myocardial infarction, liposomes for cancer chemotherapy, gold nanorods for tumor therapy, and chitosan for gene therapy.[25–28] Notably, MCM-41 exhibits exceptional structural regularity with its hexagonal pore architecture ensuring uniform pore size distribution (2–10 nm), which enhances loading precision and release kinetics control compared to less ordered materials. Its high thermal and mechanical stability under physiological conditions further expands its applicability in complex delivery systems.[29] Additionally, MCM-41's air tolerance during synthesis simplifies manufacturing processes while maintaining structural integrity, making it particularly advantageous for scalable production of advanced drug carriers.

In this research, we showcase a development of a spontaneous drug delivery system for addressing various postoperative complications following open fracture surgeries. By integrating acrylamide-acrylic acid copolymer with drug-laden MCM-41, a renowned MSN, we synthesized the nanoporous medical composite hydrogel (NMCH) through a straightforward physical mixing and light curing technique. In contrast to conventional pharmacotherapies and *in situ* treatments, NMCH ensures a sustained and stable release of medication at the treatment site over an extended period. Specifically targeting bacterial infection, retarded bone cell growth, and inflammation, we formulated three distinct NMCH variants as spontaneous delivery platforms. These were loaded with vancomycin (Van), dexamethasone (Dex), and celecoxib (Cel), denoted as NMCH@Van, NMCH@Dex, and NMCH@Cel, respectively. We conducted thorough investigations into their structures, morphologies, BET surfaces, and drug release profiles. Furthermore, we assessed their antimicrobial efficacy and performed *in vitro* pharmacodynamic evaluations for postoperative treatment of open fractures. Notably, NMCH maintained a prolonged and stable drug release throughout the therapeutic period, coupled with mechanical properties that surpassed those of the periosteum.

2. Experimental section

2.1 Material

DMEM medium (No. PM150210) was purchased from Punosai. Australian Premium fetal bovine serum (iCell-0500) was purchased from Cybkang. Trypsin-EDTA digest (0.25%) containing phenol red (No. T1320) was purchased from Solarbio. CCK-8 cell proliferation detection kit was purchased from Kulaibo. BMSC cells were purchased from Sabachem Biotechnology Co. The rest were purchased from Macklin.

2.2 Characterization

X-ray diffraction analysis was carried out on a German Brook D8 advance. Transmission electron microscopy analysis was performed on a American FEI TecnaiG20. The FT-IR spectrum was measured on a Thermo Fisher Technology Nicolet 6700. The double-column electronic tensile testing machine (I5965) was purchased from Instron (Shanghai) Testing Equipment Co. Scanning electron microscopy analysis was carried out on a Czech TESCAN VEGA 3 SBH. Double Column Electronic Tensile The UV-vis spectrum was measured on Shimadzu UV3600. High temperature and pressure steam sterilization pot (HVE-50) was purchased from Hirayama. Multi-function microplate reader (TECAN SPARK 10M) was purchased from Ruishang. Clean bench (SW-CJ-2FD) was purchased from Sujing Antai. Constant temperature oscillator (crystal IS-RDV1) was purchased from American Jingqi.

2.3 Synthesis of MCM-41

The synthesis of MCM-41 with different pore size was based on a previous study.[30] 0.3 g cetyltrimethylammonium bromide was dissolved in a mixture of 32.5 g of water and 22.5 g of ammonia and stirred at 40 °C until completely dissolved. The stirring was then continued for 1 h in the presence or absence of TMB. 1.18 g of tetraethyl orthosilicate (TEOS) was added drop by drop to the mixed solution and stirred for 6 h at room temperature. The precursors were then transferred to a Teflon-lined stainless-steel autoclave and crystallized for 72 h at 120 °C. The crystallized mixture was centrifuged to separate the white solid and washed until the centrifuged supernatant was neutral, and the washed white solid was dried at 80 °C. To remove the surface-active template agent, the dried product was heated from room temperature to 550 °C at a heating rate of 5 °C min^{-1} and roasted in air for 6 h. Finally, MCM-41 white powder with different pore size were obtained and named MCM-41-*n* ($n = 0$, 0.1, 0.2, 0.3,0.4 g TMB).

2.4 Preparation of medicine stock solution

1.0 g of Van was dissolved in 20 mL water and stirred at 30 °C for 20 min to obtain MINO aqueous solution with a concentration of 50 mg mL^{-1}. After diluted with water, various concentrations of 10–50 mg L^{-1} Van aqueous solution were obtained. The maximum wavelength (λ_{max}) of Van is 280 nm; 0.10 g of Dex was dissolved in 10 mL ethanol and stirred at 30 °C for 20 min to obtain Dex ethanol solution with a concentration of 10 mg mL^{-1}. After diluted with ethanol, various concentrations of 1–10 mg L^{-1} Dex aqueous solution were obtained. The λ_{max} of Dex is 242 nm; 0.50 g of Cel was dissolved in 10 mL ethanol and stirred at 30 °C for 20 min to obtain Cel ethanol solution with a concentration of 50 mg mL^{-1}. After diluted with ethanol, various concentrations of 10–50 mg L^{-1} MCZ aqueous solution were obtained. The λ_{max} of MCZ is 208 nm.

2.5 Medicine loading

MCM-41 loaded with medicines was obtained by solvent impregnation method. Taking the load of Van as an example, 0.5 g MCM-41-0.4 was added to 10 mL of Van aqueous solution with a concentration of 50 mg mL^{-1}, and the suspension was stirred vigorously at room temperature for 48 h to achieve an equilibrium steady state. Then the suspension was centrifuged at 9000 rpm for 15 min. The supernatants were collected and extracted into quartz colorimetric ware with a 0.22 μm filter syringe. After adequately diluted, the loading capacity of Van was measured by UV-vis spectrophotometer. The solid was kept at 60 °C for 24 h for solvent evaporation and is hereafter referred to as MCM-41-0.4@Van. Same methods were used to load Dex and Cel. The Dex drug-loaded solution is an ethanol solution with a concentration of 1 mg mL^{-1}. The Cel drug-loaded solution is an ethanol solution with a concentration of 50 mg mL^{-1}. Based on the different molecular sizes of these two drugs, we chose MCM-41 with different pore sizes, named as MCM-41-0.2@CA and MCM-41-0.2@MCZ.

2.6 Preparation of PAAm-AAc

The synthetic equation of PAAm-AAc is shown in Fig. S1a.† 6 g acrylamide (AAm), 1.2 g acrylic acid (AAc) as monomer, 0.02 g photo initiator TPO, and 0.02 g poly (ethylene glycol) diacrylate as cross-linking agent were mixed in 20 mL of deionized water, and dissolved by thorough stirring to produce the precursor solution. The precursor solution was poured into a polytetrafluoroethylene mold (100 × 100 × 5 mm) and purged with N_2 for 20 min. Finally, the PAAm-AAc hydrogel was obtained after the precursor solution was irradiated by UV light for 60 s.

2.7 Preparation of NMCHs

0.1 g of the above drug-carrying MCM-41-*n* was mixed with a certain proportion of hydrogel precursor solution, and ultrasonication was performed for 15 min to make the mixture homogeneous and remove air bubbles. The mixed solution was placed in a polytetrafluoroethylene mold (100 × 100 × 5 mm) and irradiated by UV light for 60 s for curing. After curing, the samples were cut into appropriate sizes with a cutter according to the test requirements. The resulting samples were named NMCH-*n*@Van, NMCH-*n*@Cel, NMCH-*n*@Dex, and NMCH-*n*@Dex.

2.8 *In vitro* medicine release study.

To determine the release trend of medicine from the NMCHs, the wafer samples were accurately weighed and soaked in a sealed colorimetric ware containing 3 mL PBS (pH = 7.2). The medicine released was analyzed by UV-vis spectrophotometer every 30 min at maximum absorption wavelength determined. Medicine release was observed over 7 days. All experiments were performed in triplicate and results were reported as an average. The percentage of medicine released was determined by below

$$\text{Percentage of medicine release } (\%) = \frac{Q_t}{Q_0} \times 100\%$$

where Q_t is the cumulative amount of medicine released at time and Q_0 is the initial amount of medicine loaded. Measurements are made at room temperature under static conditions.

2.9 Solvent swelling-drying cycle experiment

The lyophilized NMCH sample was immersed in PBS (37 °C) until swelling equilibrium was reached, and the mass after swelling was recorded. In the drying phase, vacuum drying (40 °C) was performed until a constant weight was achieved, and the mass loss was calculated. This cycle was repeated 5–10 times.

2.10 Antibacterial activity

The antibacterial properties of vancomycin hydrochloride-loaded NMCH were determined by diffusion method using *Staphylococcus aureus* as the experimental strain. For OD measurements, optical density was monitored at specific time windows: 6 h for *E. coli* incubation and 12 h for *S. aureus* incubation to capture logarithmic growth phase. 3 mL of Luria-Bertani (LB) liquid medium was added to a 12 mL bacterial culture tube, and single colonies were picked from the solid medium of *S. aureus* and added to the tube, which was placed in a thermostatic oscillator at 200 rpm at 37 °C and incubated overnight. Control groups included sterile LB medium as blank control and untreated bacterial suspensions as positive control to establish baseline growth parameters. The *E. coli(ATCC 25922)* and *S. aureus (ATCC 29213)* colonies were diluted with sterile PBS solution until a concentration of 10^6 CFU mL^{-1} was reached. Subsequently, 100 μL of the bacterial solution was accurately aspirated and spread evenly on the surface of LB solid medium. Next, a 6.0 mm diameter hole punch was used to punch holes in the medium. After punching the holes, the sterilized samples were carefully placed into the medium holes. After that, the whole Petri dish was placed in an incubator at a constant temperature of 37 °C for 24 h of incubation. At the end of incubation, the Petri dish was taken out, photographs were taken using an ordinary camera, and the size of the ring of inhibition was measured and recorded.

2.11 *In vitro* cell propagation experiment

BMSC cells in logarithmic growth phase were seeded at a density of 1×10^4 cells per well in 96-well plates. After 12 hours of incubation at 37 °C with 5% CO_2, the cells were divided into three groups: (1) untreated, (2) treated with PAAm-AAc, and (3) treated with PAAm-AAc@Dex. Each group's samples (1 g) were immersed in 10 mL of medium for 24 h, followed by filtration through a 0.22 μm membrane to obtain the sample extracts at a concentration of 0.1 g mL^{-1}. These extracts were then diluted with medium to prepare a series of gradient concentrations (20%, 40%, 60%, and 80% wt%). The cells were treated with these dilutions and co-cultured for 24 h and 72 h. After incubation, cells were washed with PBS three times, and 100 μL of culture medium containing CCK-8 solution was added to each well. The plates were subsequently incubated at 37 °C with 5% CO_2 for an additional 2 h.

2.12 Rat Paw Edema Experiment

The samples are divided into three groups: non-drug-loaded PAAm-AAc (Group A), celecoxib-loaded PAAm-AAc (Group B), and NMCH@Cel (Group C). Groups B and C have the same drug loading, and all samples undergo 12 hours of dialysis before extraction to remove un-crosslinked monomers. All samples are sterilized by UV light for 4 hours. After one week of acclimatization, the thickness of the left hind paws of male rats is measured using a caliper. Administer 0.1 mL of 3% carrageenan to induce inflammation and calculate paw swelling. Inject 0.05 g of each sample into the left hind paw and measure paw thickness hourly for 8 hours. Perform each group in triplicate.

Calculate swelling percentage as follows:

$$\text{Swelling} \quad (\%) \ = \frac{V - V_{\text{i}}}{V_{\text{i}}} \times 100\ \%$$

where V is the paw thickness at each time point and V_{i} is the paw thickness before carrageenan injection.

Compare the average paw swelling in drug-treated rats with that in the control group (receiving placebo gel) using the following formula:

$$\text{Inhibition} \quad (\%) = \frac{1 - [\text{swelling}]\_\text{treated}}{[\text{swelling}]\_\text{control}} \times 100\%$$

where swelling_treated is the average paw swelling observed in the experimental group, and swelling_control is the average paw swelling observed in the control group.

All protocols in this study were approved by the Committee on the Ethics of Animal Experiments of Yuanxuan Biotechnology (Hangzhou) Co., Ltd, with ethical oversight relevant to the conduct of the study (IACUC permit number: YXSW2310112797). The study was conducted in compliance with the Guide for the Care and Use of Laboratory Animals published by the US National Institutes of Health (NIH publication No. 85-23, revised 1996).

2.13 Statistical analysis

The data was expressed as mean ± standard deviation (SD). Statistical analysis was performed with SPSS 22.0 (SPSS, Inc., Chicago, IL, USA). The two-group and multiple-group statistical analysis were compared by single-factor analysis of variance (ANOVA) and *t*-test. $P < 0.05$ was considered to be statistically significant.

3. Results and discussion

3.1 Synthesis and characterization

Schematic diagram of NMCH components and their combinations were shown in Fig. S1b,† MCM-41 and drug molecules are uniformly encapsulated in a PAAm AAc cross-linked network. The structures of samples were recorded by the characterization methods of TEM and XRD. Fig. 1A and E showed the TEM image of the pure MCM-41 sample. It captured perpendicular to the material's pores, clearly revealing its ordered long straight channels. The diameter of MCM-41 was measured 2.1 nm. Fig. 1B–D respectively presented the images of MCM-41 infusing with Vancomycin (Van), Dexamethasone (Dex), and Celecoxib (Cel). The incorporation of drugs did not damage the ordered pore structure of MCM-41, but the diameters of MCM-41 were measured 2.5, 2.6 and 2.3 nm, which meant that the pores were expanded after infusion. There was no obvious aggregation of particles observed. The XRD patterns of the materials were shown in Fig. S2.† Fig. S2a† displayed five curves with adding 0 g, 0.1 g, 0.2 g, 0.3 g and 0.4 g TMB as expanding agents during the synthetic procedure. They had a strong peak at 2θ between 2.2 and 2.6°, and this peak could be indexed to the (100) surface of the well-ordered hexagonal MCM-41 structure. As the amount of expanding agent TMB increased, the lattice constant became larger, thus the peak had a left shift. Fig. S2b–d† displayed five curves which corresponded to Van, Dex, and Cel infusing in MCM-41 respectively. Every curve had the feature peaks of MCM-41. Lower intensity than original samples reflected the effect of medicine infusion, illustrating that the medicine entered the pores successfully but did not damage the porous structures. The overall morphology of these samples was also recorded by TEM (Fig. 1E–H). The original MCM-41 samples had an irregular spheroidal shape, and the morphology did not change after drug injection (Table 1).

The states of surface groups on all involved compounds[31–33] and as-prepared materials were recorded by a Fourier transform infrared spectrometer (FT-IR). Fig. 2A showed the standard IR spectra of three medicine molecules. As seen, vancomycin had a wide spectra band at 3470 cm^{-1} caused by O–H stretching and a bank at 1635 cm^{-1} caused by C=O vibration. For dexamethasone, the broad band at 3460 cm^{-1} was attributed to O–H stretching, and the absorption bank from 3000 cm^{-1} to 2800 cm^{-1} was caused by the C–H stretching of the sp^3 hybridized carbon. C=O in Dex was coupled with C=C, so an absorption peak at 1618 cm^{-1} was observed. The tensile and axial deformation bands of the C–F bond could be observed at 1139 cm^{-1} and 887 cm^{-1} respectively. The stretching vibration of N–H in celecoxib was in the range of 3200–3300 cm^{-1}, and the peaks locating around 1471 and 1284 cm^{-1} were corresponded with C=C and C–F bonds. Fig. 2B showed the characteristic IR spectra of base material MCM-41 and the graft states after medicine loading into the pores of MCM-41. MCM-41 had peaks located at 997–1145 cm^{-1}, which could be attributed to the asymmetric stretching vibration of the Si–O–Si bond. When the medicines were infused into MCM-41 pores, the featured absorption peaks of the composite perfectly matched that of pure MCM-41, but all the characteristic peaks of medicines vanished nearly, which indicated that the absorption of medicine in MCM-41 led to the connection of almost all the N–H and O–H in medicine molecules and the Si–OH groups of MCM-41.

The structure of PAAm-AAc and the drug delivery systems that combines PAAm-AAc and MCM-41@medicines (NMCH) were recorded by SEM and IR. Fig. S4A† displayed the SEM pattern of PAAm-AAc showing a flat surface and some vertical lines. Fig. S4B† showed the record of NMCH. The surface of NMCH became rough and formed a spongy-like bump upwards. It was inferred that the introduction of MCM-41 might have changed the network structure of the hydrogel to some extent.

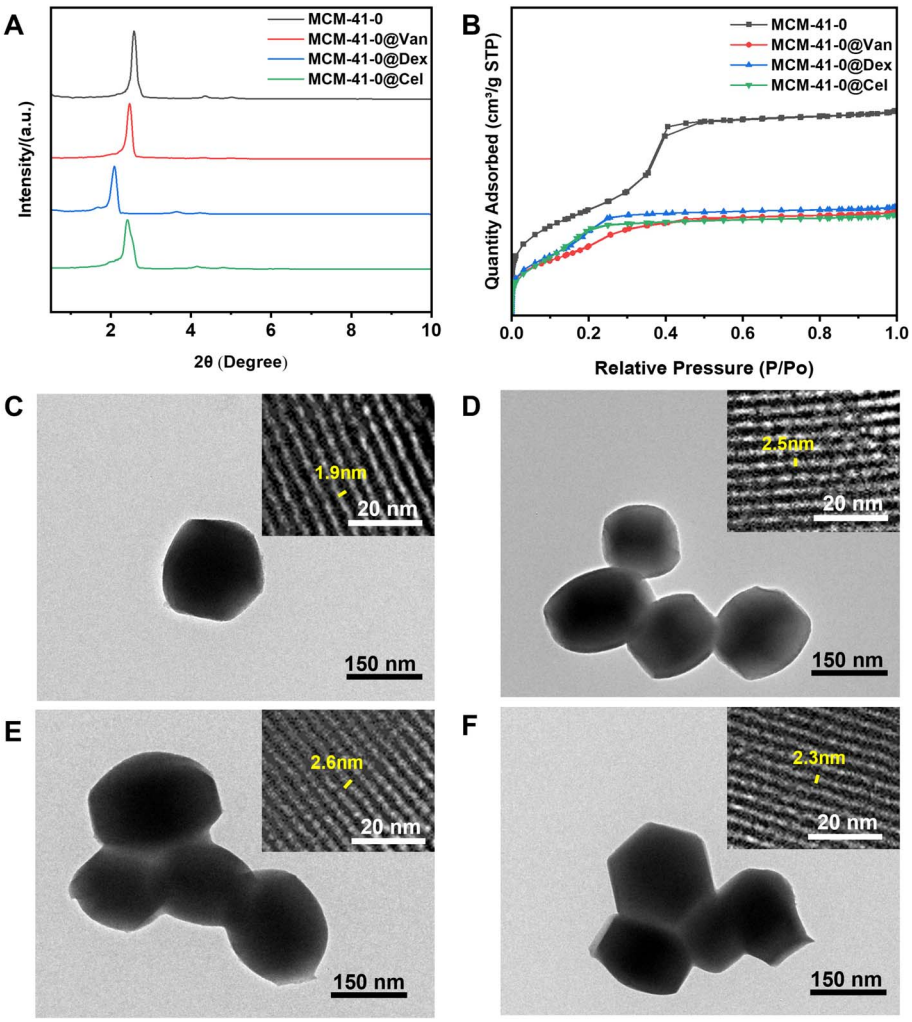

Fig. 1 (A) XRD patterns of MCM-41-0, MCM-41-0@Van, MCM-41-0@Dex and MCM-41-0@Cel, (B) N_2 adsorption–desorption isotherms of MCM-41-0, MCM-41-0@Van, MCM-41-0@Dex and MCM-41-0@Cel, TEM image of (C) MCM-41-0, (D) MCM-41-0@Van, (E) MCM-41-0@Dex, (F) MCM-41-0@Cel.

The comparison of IR patterns of MCM-41, PAAm-AAc and NMCH were shown in Fig. 2C. The characteristic peak of Si–O vibration in MCM-41 appeared near 1030 cm^{-1}, and a broad peak appeared at approximately 3448 cm^{-1} for the PAAm-AAc hydrogel, corresponding to the stretching vibration of N–H. After their combination, their respective characteristic peaks were retained, but the intensity of the peak of MCM-41 decreased, presumably due to being encapsulated by PAAm-AAc. Fig. 2D displayed the IR spectra of three drug delivery systems combining PAAm-AAc and MCM-41@medicines. Only the characteristics of the hydrogel could be indexed. Combining these IR spectra with the SEM observation results (Fig. 2A and B), MCM-41@medicines should be completely encapsulated by the hydrogel.

3.2 Adjustment of mechanical capacity

Hydrogel materials have demonstrated their unique potential for use in orthopedic implantation surgery, especially as their mechanical properties can be flexibly regulated by adjusting the ratio of the constituent monomers.[34] Fig. 3A showed the stress–strain curves exhibited by hydrogels at various AAm/AAc ratios, and Fig. 3B showed the tensile strength at the moment of fracture with the corresponding elongation of hydrogels at various AAm/AAc ratios. According to Fig. 3A and B, it could be

Table 1 Physicochemical properties of MCM-41 with and without medicine loading

Samples	MCM-41-0	MCM-41-0.4	MCM-41-0.4@Van	MCM-41-0@Dex	MCM-41-0@Cel
Surface area(m^2 g^{-1})	1339	1037	779	1141	981
Pore size (nm)	1.9	2.7	2.5	2.6	2.3

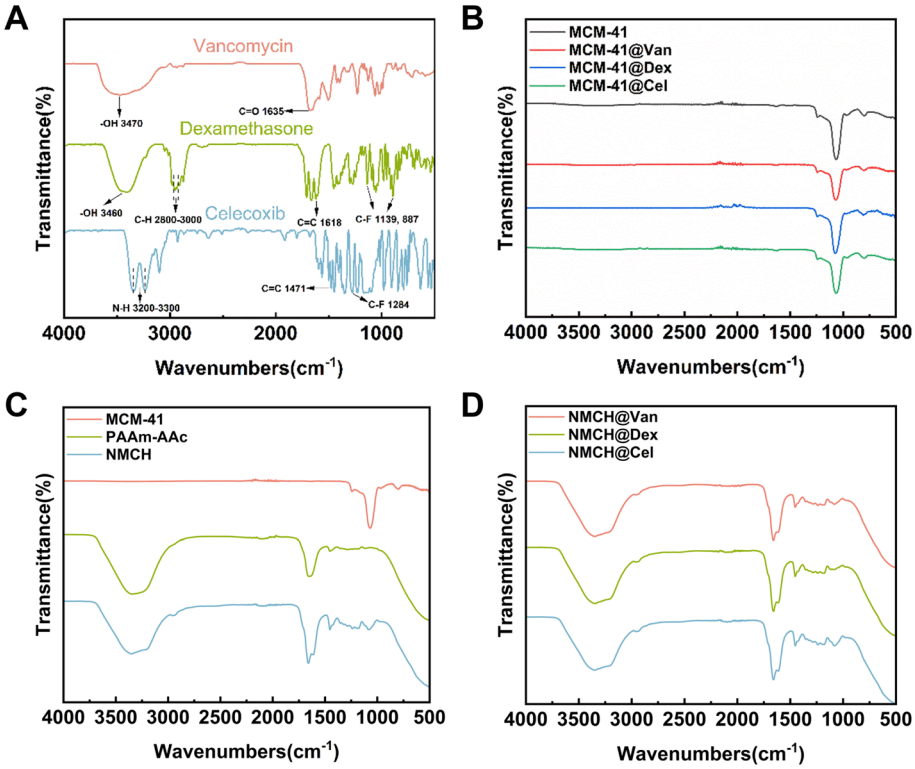

Fig. 2 FT-IR spectra of (A) three kinds of medicines with featured absorptions, (B) MCM-41-0 loading Van, Dex and Cel., (C) MCM-41, PAAm-AAc and NMCH, (D) NMCH containing different medicines.

found that the prepared PAAm-AAc hydrogels exhibited the most desirable combination of mechanical properties when the ratio of AAm to AAc was accurately set to 2 : 1. The hydrogel in this ratio not only possessed a tensile strength of 0.24 MPa, but also an elongation at break of 342.79%. This excellent mechanical performance lay a solid foundation for subsequent experimental studies and practical applications. On this basis, to further explore and optimize the performance of the carrier, MCM-41 was introduced into the optimized hydrogel system (AAm/AAc = 2 : 1). By precisely controlling the amount of MCM-41 added, the optimal formulation that could maintain the hydrogel's excellent mechanical properties while effectively enhancing drug delivery efficiency was identified. As shown in Fig. 3C, when the addition of MCM-41 reached 0.5 wt%, the NMCH material exhibited the best elongation at break (1141.8%) and maximum strength (0.31 MPa), indicating effective interaction and dispersion between MCM-41 and the PAAm-AAc hydrogel, which improved the overall mechanical properties of the composite material. To intuitively assess the practical application potential of the NMCH carrier, their mechanical properties with those of natural periosteum stripped from pig leg bones was compared. As illustrated in Fig. 3C and D, the optimized NMCH carrier significantly surpassed the pig periosteum in both elongation at break (1141.8% *vs.* 439.1%) and strength (0.31 MPa *vs.* 0.24 MPa). This finding not only confirmed the successful design of our NMCH carrier but also provided a solid scientific foundation and broad prospects for its application in orthopedic treatment, tissue engineering, and other related fields.

3.3 Cyclic stability analysis

Swelling-drying equilibrium experiments are essential for evaluating hydrogel stability by quantifying their resistance to structural degradation during repeated hydration cycles. As Table S1† indicates, NMCH hydrogels reinforced with MCM-41 nanoparticles showed marked improvements in dimensional stability, with mass loss rates below 6%, whereas unmodified PAAm-AAc hydrogels exhibited significantly higher degradation exceeding 9%. This contrast emphasizes that MCM-41's porous structure enhances cross-linking efficiency and water retention, thereby suppressing irreversible chain scission and matrix collapse. The substantial reduction in mass loss for NMCH underscores its reliability as a stabilized hydrogel system capable of withstanding cyclic environmental stresses.

3.4 *In vitro* studies on sustained medicine release

In the tests for MCM-41-0.1@Van and hydrogel@Van loaded with drug alone, it was observed that both of them suffered from rapid drug release. As can be seen in Fig. 4A, MCM-41-0.1@Van dissolved rapidly within three hours, reaching 49.6% drug release; similarly, hydrogel@Van also released 55.1% drug rapidly. Although this rapid release can quickly reach the therapeutic concentration at the initial stage, it is not conducive to the long-term stabilization and sustained release of the drug. To address this issue, a combination of MCM-41-0.1 and hydrogel was considered. By thoughtful design, the advantages of both can be fully utilized to compensate for the shortcomings of each. The addition of hydrogel provides a controlled-release layer for MCM-

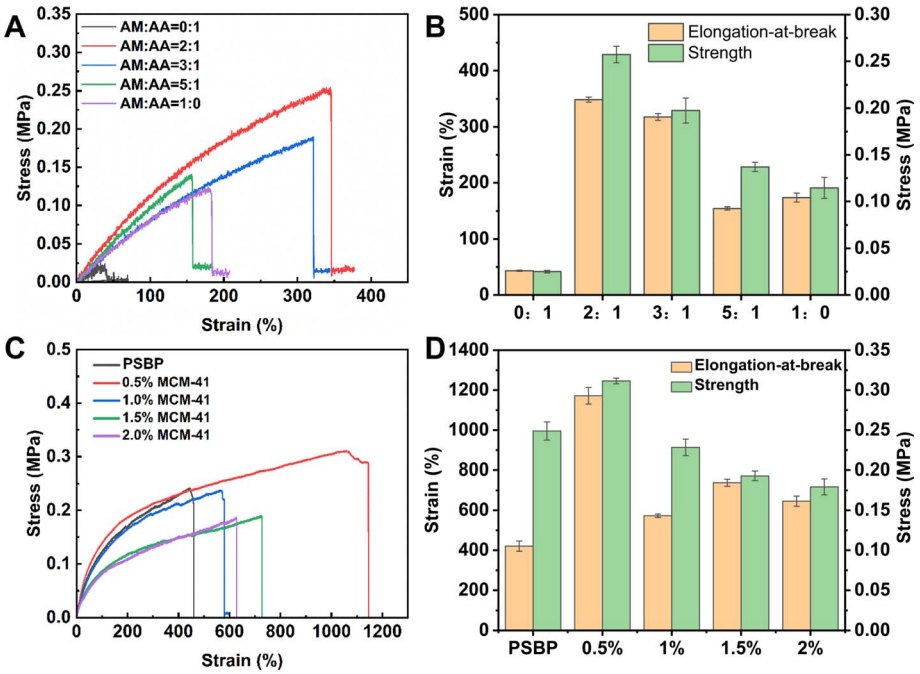

Fig. 3 PAAm-AAc with different monomer ratios: (A) stress–strain curves, (B) strength and elongation at break, NMCH with different MCM-41 ratios: (C) stress–strain curves, (D) strength and elongation at break.

41-0.1, which utilizes its swelling and water-release properties to slow down the release of the drug; while the pore structure of MCM-41-0.1 helps the drug to be evenly distributed in the hydrogel, which improves the release stability and bioavailability.

The releasing behaviors of Van, Cel, and Dex molecules from NMCHs were investigated in phosphate buffer (PBS) at pH 7.2, respectively. Fig. 4B–D showed the release profiles of different drugs (Van, Cel, and Dex) over time, respectively. In these three

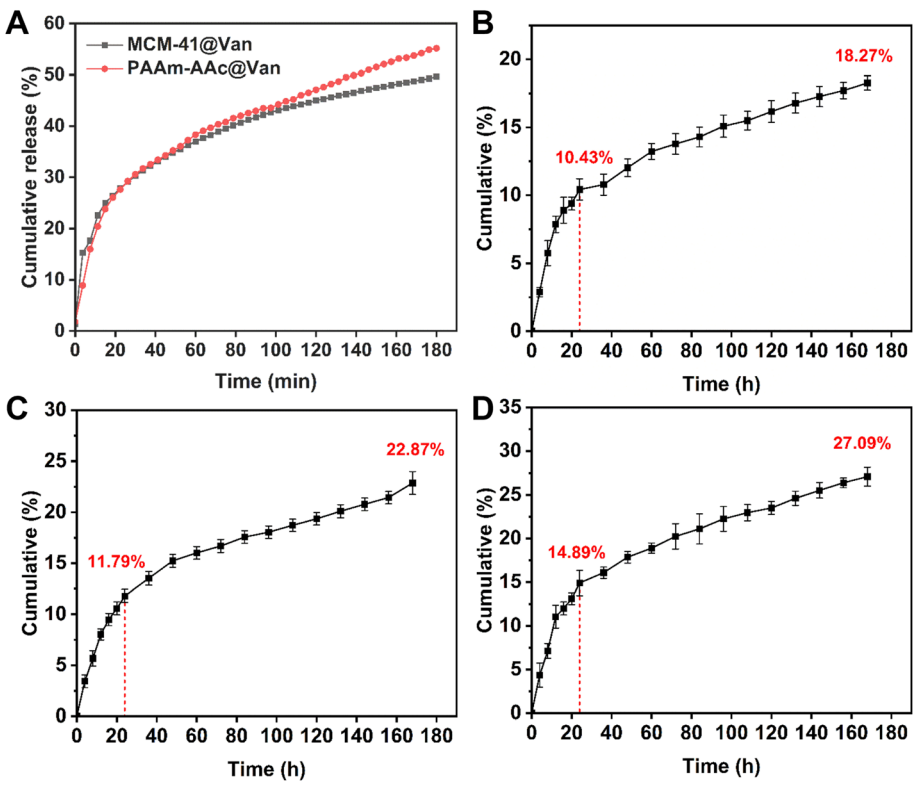

Fig. 4 *In vitro* medicine release profile of (A) MCM-41@Van (black line) and PAAm-AAc@Van, (B) NMCH@Van, (C) NMCH@Dex and (D) NMCH@Cel.

figures, it could be observed that all three drugs exhibited a similar two-phase release pattern during the 168-hours-long monitoring period. Within 24 hours of starting the experiment, there was a significant rapid release process in which approximately 10.43% of Van, 11.79% of Cel, and 14.89% of Dex were rapidly released from the NMCH carrier into solution. After this rapid release phase, all three drugs entered a prolonged and sustained slow-release phase. During this period, the concentration of the drugs in solution gradually increased at a steady rate, corresponding to the slow and sustained upward trend in the release profile. Even at the 168th hour of the experiment, the cumulative amount of drug released was only 18.27% of Van, 22.87% of Cel, and 27.09% of Dex, indicating that the NMCH carrier exhibited good performance in slow drug release and was capable of maintaining effective drug release over a long period.

The pH-responsive release behavior of NMCHs was further analyzed by comparing drug release profiles at pH 6.4 and pH 7.2 (Fig. S3†). Interestingly, the release rate at pH 7.2 was slightly higher than that at pH 6.4, which we hypothesize is due to the protonation of amide groups in the PAAm-AAc chains under acidic conditions. This protonation likely induces chain contraction, partially blocking the mesoporous channels of MCM-41 and thereby reducing drug release. This characteristic is advantageous for scenarios where increased drug release is desired during the early alkaline phase of tissue inflammation, followed by reduced release as immune cells secrete acidic substances, creating a localized acidic environment. Such pH-sensitive modulation enhances the precision of drug delivery, aligning with the dynamic physiological changes in inflamed tissues.

3.5 *In vitro* and *in vivo* evaluation of antibacterial activity, cell proliferation, and periodontitis

Using both *Staphylococcus aureus* (a known pathogen that can cause chronic osteomyelitis) and *Escherichia coli* (a common Gram-negative bacterium) as test bacteria, a blank control was established to monitor the antibacterial effect of NMCH@Van over 36 hours. In the following antibacterial experiments, all materials containing MCM-41 used MCM-41-0.4 to ensure that the drug loading was sufficient to achieve antibacterial effects. The results described in Fig. 5A–C indicated that NMCH@Van exhibited a time-dependent increase in the diameter of the inhibition zone for both bacteria, from 11 millimeters to 13 millimeters for *Staphylococcus aureus* and from 10 millimeters to 12 millimeters for *Escherichia coli*, suggesting that NMCH@Van had a significant inhibitory effect on both types of bacteria.

The biocompatibility of biomaterials is crucial for potential applications in bone tissue engineering. Firstly, the cytotoxicity of the PAAm-AAc hydrogel extract, MCM-41, and drug-loaded NMCHs was assessed. We evaluated the cytotoxicity of various concentrations of the hydrogel extracts on BMSCs using the CCK-8 method. The results demonstrated that the overall cell viability remained above 90%, indicating that the NMCHs were non-cytotoxic. Fig. 5D–F showed the effects of PAAm-AAc,

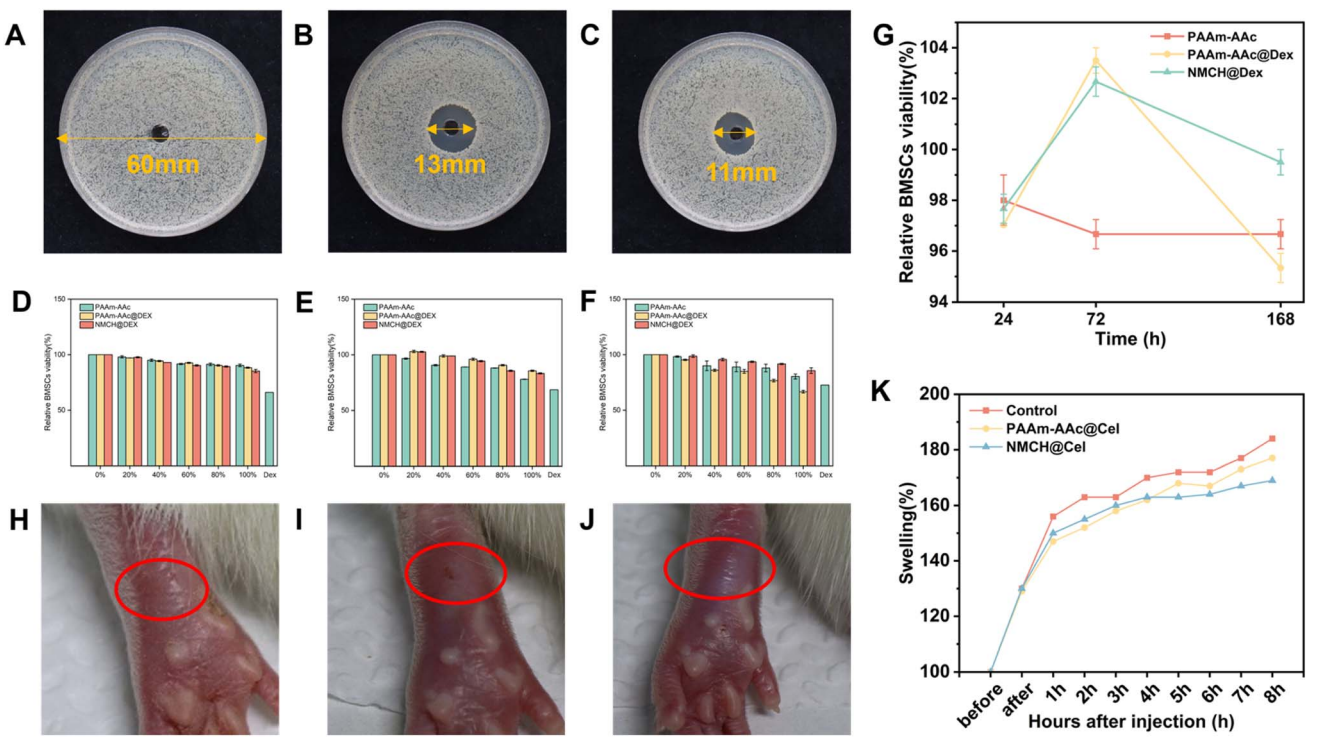

Fig. 5 *In vitro* antibacterial of NMCH@Van (A) 0 h, (B) 12 h, and (C) 36 h; *in vitro* BMSC cell proliferation of PAAm-AAc, PAAm-AAc@Dex and NMCH@Dex (D) 24 h, (E) 72 h, (F) 168 h, (G) Time Trend Chart of *in vitro* BMSC cell proliferation; Photo of Rat Paw Edema experiment, (H) PAAm-AAc, (I) PAAm-AAc@Cel, (J) NMCH@Cel; (K) swelling rate and inhibition Rate of Rat Hind Paw. $^{*}P < 0.05$, $^{**}P < 0.01$.

dexamethasone-loaded PAAm-AAc (PAAm-AAc@Dex), and NMCH@Dex on the proliferation of BMSC cells at the time points of 1, 3, and 7 days, respectively. Fig. 5D displayed that the relative BMSC cell viability remained above 80% in all groups during the 24-hours incubation period, indicating that PAAm-AAc and NMCH were well biocompatible with BMSC cells. By day 3, as shown in Fig. 5E, the relative cell viability of both the PAAm-AAc group containing dexamethasone and the NMCH@Dex group had been significantly higher than that of the PAAm-AAc control group without dexamethasone, confirming that dexamethasone had a significant growth-promoting effect on BMSC cells, which was beneficial to cell proliferation and differentiation. When the samples had been co-cultured with BMSC cells for 7 days, it revealed that NMCH@Dex exhibited optimal pro-cell proliferative capacity (Fig. 5F). Fig. S5† provides fluorescence microscopy images of the cells, which corroborate the cell proliferation data. Fig. 5G compared the changes in the pro-growth effects of PAAm-AAc@Dex and NMCH@Dex on BMSC cells during the 7-days treatment. The results showed that during the first three days, PAAm-AAc@Dex had a slightly superior growth-promoting effect, which was attributed to the faster release of dexamethasone from the MCM-41-free drug-carrying hydrogel. However, when treatment was extended to 7 days, PAAm-AAc@Dex was unable to maintain effective drug concentrations in the later stages due to the rapid release of the drug in the earlier stages. In contrast, although NMCH@Dex was slightly less effective than PAAm-AAc@Dex in cell proliferation in the first 3 days, it was able to maintain a more stable drug concentration in the subsequent 7 days. In addition, a side-by-side comparison of cell proliferation at different proportional concentrations of the same samples in Fig. 5D–F showed that as the concentration of dexamethasone increased, the proliferation of BMSC cells was instead inhibited, which indicated that the concentration of dexamethasone had a dual effect on cell proliferation and needed to be used in an appropriate range to achieve the best effect. While the current focus on cellular-level biocompatibility establishes fundamental safety parameters, future studies will implement GLP-compliant 90-days implantation models with comprehensive histopathological analysis and serum cytokine profiling, following the protocol framework validated in recent AD therapy trials.

Paw edema experiments were performed on SD rats. Fig. 5H–J showed photos of the paw edema experiment after injection of different samples. Red circles marked the affected areas after injection of different samples following the induction of edema. Fig. 5K illustrated the time-course of edema percentage and swelling inhibition percentage for PAAm-AAc@Cel and NMCH@Cel. After inducing acute inflammation with carrageenan in the control group, significant increase in paw thickness were observed around 1 hour. Within the first 4 hours after carrageenan injection, PAAm-AAc@Cel showed better edema inhibition compared to NMCH@Cel, indicating a higher drug release rate in the short term. After 4 hours, NMCH@Cel began to show better edema inhibition compared to PAAm-AAc@Cel, suggesting that NMCH@Cel provided a more sustained therapeutic effect over a longer period. At the end of the experiment, NMCH@Cel exhibited a higher edema inhibition rate than PAAm-AAc@Cel.

4. Conclusions

In conclusion, we developed a nanoporous medicine composite hydrogel (NMCH) as a spontaneous drug delivery platform by combining hydrogel and mesoporous silica nanoparticles. The platform promoted drug diffusion from a dual system (mesoporous straight channel of MCM-41 and cross-linked network of hydrogel), which significantly prolonged the drug release time and improved the mechanical properties by adjusting the ratio of monomer to MCM-41. In the postoperative phase of open orthopedic surgery, the developed Van/Dex/Cel-loaded NMCH had excellent antimicrobial, anti-inflammatory, and osteoclast proliferation properties. It can be used as a postoperative therapeutic adjuvant to prevent bacterial infections, osteoclast growth retardation, and wound inflammation. It is expected that NMCH has a broad clinical application in the treatment of open trauma and extensive suture surgery.

Data availability

The data supporting this article have been included as part of the ESI.†

Conflicts of interest

There are no conflicts to declare.

Acknowledgements

This work was supported by the National Key Research and Development Program of China (Grant No. 2022YFA1503600) and Jiangsu Shuangchuang Doctor Program (JSSCBS20210676). The authors also thank Miss. Shihui Zheng, Ms. Qingxin Niu for their technical support and some helping bio-tests from SHIYANJIA lab.

References

1 Q. Hu, Y. Zhao, B. Sun, W. Qi and P. Shi, *Int. Wound J.*, 2020, **17**, 708–715.
2 D. J. Hunter and S. Bierma-Zeinstra, *Lancet*, 2019, **393**, 1745–1759.
3 Y. Liang, X. Zhao, T. Hu, B. Chen, Z. Yin, P. X. Ma and B. Guo, *Small*, 2019, **15**, e1900046.
4 C. M. Court-Brown, C. S. Honeyman, N. D. Clement, S. A. Hamilton and M. M. McQueen, *Injury*, 2015, **46**, 2443–2447.
5 F. Loi, L. A. Córdova, J. Pajarinen, T. H. Lin, Z. Y. Yao and S. B. Goodman, *Bone*, 2016, **86**, 119–130.
6 W. G. Yang, C. T. Chen, P. K. Tsay and Y. R. Chen, *J. Trauma*, 2002, **52**, 498–503.
7 H. Rao, *J. Foot Ankle Surg.*, 2012, **51**, 209–211.
8 B. Loh, J. A. Lim, M. Seah and W. Khan, *J Perioper Pract.*, 2022, **32**, 100–107.

9 D. Campoccia, L. Montanaro and C. R. Arciola, *Biomaterials*, 2006, **27**, 2331–2339.
10 H. K. Li, I. Rombach, R. Zambellas, A. S. Walker, M. A. McNally, B. L. Atkins, B. A. Lipsky, H. C. Hughes, D. Bose, M. Kümin, C. Scarborough, P. C. Matthews, A. J. Brent, J. Lomas, R. Gundle, M. Rogers, A. Taylor, B. Angus, I. Byren, A. R. Berendt, S. Warren, F. E. Fitzgerald, D. J. F. Mack, S. Hopkins, J. Folb, H. E. Reynolds, E. Moore, J. Marshall, N. Jenkins, C. E. Moran, A. F. Woodhouse, S. Stafford, R. A. Seaton, C. Vallance, C. J. Hemsley, K. Bisnauthsing, J. A. T. Sandoe, I. Aggarwal, S. C. Ellis, D. J. Bunn, R. K. Sutherland, G. Barlow, C. Cooper, C. Geue, N. McMeekin, A. H. Briggs, P. Sendi, E. Khatamzas, T. Wangrangsimakul, T. H. N. Wong, L. K. Barrett, A. Alvand, C. F. Old, J. Bostock, J. Paul, G. Cooke, G. E. Thwaites, P. Bejon, M. Scarborough and O. T. Collaborators, *N. Engl. J. Med.*, 2019, **380**, 425–436.
11 E. A. Masters, R. P. Trombetta, K. L. D. Bentley, B. F. Boyce, A. L. Gill, S. R. Gill, K. Nishitani, M. Ishikawa, Y. Morita, H. Ito, S. N. Bello-Irizarry, M. Ninomiya, J. D. Brodell, C. C. Lee, S. P. Hao, I. Oh, C. Xie, H. A. Awad, J. L. Daiss, J. R. Owen, S. L. Kates, E. M. Schwarz and G. Muthukrishnan, *Bone Res.*, 2019, **7**, 20.
12 X. Shen, Z. Zhang, C. Cheng, C. Liu, N. Ma, D. Sun, D. Li and C. Wang, *Biomed. Technol.*, 2024, **5**, 87–101.
13 N. Nagai, C. Yoshioka and Y. Ito, *J. Oleo Sci.*, 2015, **64**, 337–346.
14 H. S. Sohn and J. K. Oh, *Biomater. Res.*, 2019, **23**, 23–29.
15 C. Jong-Woo and K. Young-Chul, *Plast. aesthetic res.*, 2023, **10**, 59.
16 A. Luca and M. Maria Costanza, *Plast. aesthetic res.*, 2023, **10**, 16.
17 J. K. Patra, G. Das, L. F. Fraceto, E. V. R. Campos, M. D. P. Rodriguez-Torres, L. S. Acosta-Torres, L. A. Diaz-Torres, R. Grillo, M. K. Swamy, S. Sharma, S. Habtemariam and H. S. Shin, *J. Nanobiotechnol.*, 2018, **16**, 71–72.
18 S. Laurent, S. Dutz, U. O. Häfeli and M. Mahmoudi, *Adv. Colloid Interface Sci.*, 2011, **166**, 8–23.
19 S. Hua, J. He, F. Zhang, J. Yu, W. Zhang, L. Gao, Y. Li and M. Zhou, *Biomaterials*, 2021, **268**, 120590.
20 W. Yin, L. Yan, J. Yu, G. Tian, L. Zhou, X. Zheng, X. Zhang, Y. Yong, J. Li, Z. Gu and Y. Zhao, *ACS Nano*, 2014, **8**, 6922–6933.
21 L. Xue, T. Deng, R. Guo, L. Peng, J. Guo, F. Tang, J. Lin, S. Jiang, H. Lu, X. Liu and L. Deng, *Front. Bioeng. Biotechnol.*, 2022, **10**, 825339.
22 J. Shi, X. Yu, L. Wang, Y. Liu, J. Gao, J. Zhang, R. Ma, R. Liu and Z. Zhang, *Biomaterials*, 2013, **34**, 9666–9677.
23 Q. Meng, S. Zhong, L. Xu, J. Wang, Z. Zhang, Y. Gao and X. Cui, *Carbohydr. Polym.*, 2022, **279**, 119013.
24 F. Tang, L. Li and D. Chen, *Adv. Mater.*, 2012, **24**, 1504–1534.
25 D. Nie, Z. Dai, J. Li, Y. Yang, Z. Xi, J. Wang, W. Zhang, K. Qian, S. Guo, C. Zhu, R. Wang, Y. Li, M. Yu, X. Zhang, X. Shi and Y. Gan, *Nano Lett.*, 2020, **20**, 936–946.
26 J. Liu, H. Liang, M. Li, Z. Luo, J. Zhang, X. Guo and K. Cai, *Biomaterials*, 2018, **157**, 107–124.
27 H. Wang, X. Chang, Q. Ma, B. Sun, H. Li, J. Zhou, Y. Hu, X. Yang, J. Li, X. Chen and J. Song, *Bioact. Mater.*, 2023, **21**, 324–339.
28 P. Y. Zhou, Y. Xia, X. S. Cheng, P. F. Wang, Y. Xie and S. G. Xu, *Biomaterials*, 2014, **35**, 10033–10045.
29 Z. Shariatinia and N. Pourzadi, *J. Mol. Struct.*, 2021, **1242**, 130754.
30 D. Zhao, J. Feng, Q. Huo, N. Melosh, G. H. Fredrickson, B. F. Chmelka and G. D. Stucky, *Science*, 1998, **279**, 548–552.
31 M. Sun, L. Cheng, Z. Xu, L. Chen, Y. Liu, Y. Xu, D. Zhou, X. Zhang, Q. Zhou and J. Sun, *Front. Bioeng. Biotechnol.*, 2022, **10**, 826971.
32 M. Jarosz, J. Latosinski, P. Gumulka, M. Dabrowska, M. Kepczynski, G. D. Sulka and M. Starek, *Pharmaceutics*, 2023, **15**, 103–105.
33 W. M. Santos, F. P. Nóbrega, J. C. Andrade, L. F. Almeida, M. M. Conceição, A. C. D. Medeiros and F. D. Medeiros, *J. Therm. Anal. Calorim.*, 2020, **145**, 361–378.
34 W. Jiang, F. S. Hou, Y. Gu, Q. Saiding, P. P. Bao, J. C. Tang, L. Wu, C. M. Chen, C. L. Shen, C. L. Pereira, M. Sarmento, B. Sarmento, W. G. Cui and L. Chen, *Bioact. Mater.*, 2022, **12**, 169–184.